Received 11 April 2023
Revised 2 June 2023
Accepted 7 June 2023

A study on aerodynamic noise characteristics of a high-speed maglev train with a speed of 600 km/h

Jie Zhang, Yuwei Wu, Jianyong Gao, Guangjun Gao and Zhigang Yang
Key Laboratory of Traffic Safety on Track, Ministry of Education, School of Traffic and Transportation Engineering, Central South University, Changsha, China;
Joint International Research Laboratory of Key Technologies for Rail Traffic Safety, Central South University, Changsha, China and
National and Local Joint Engineering Research Center of Safety Technology for Rail Vehicle, Central South University, Changsha, China

Abstract

Purpose – This study aims to explore the formation mechanism of aerodynamic noise of a high-speed maglev train and understand the characteristics of dipole and quadrupole sound sources of the maglev train at different speed levels.

Design/methodology/approach – Based on large eddy simulation (LES) method and Kirchhoff–Ffowcs Williams and Hawkings (K-FWH) equations, the characteristics of dipole and quadrupole sound sources of maglev trains at different speed levels were simulated and analyzed by constructing reasonable penetrable integral surface.

Findings – The spatial disturbance resulting from the separation of the boundary layer in the streamlined area of the tail car is the source of aerodynamic sound of the maglev train. The dipole sources of the train are mainly distributed around the radio terminals of the head and tail cars of the maglev train, the bottom of the arms of the streamlined parts of the head and tail cars and the nose tip area of the streamlined part of the tail car, and the quadrupole sources are mainly distributed in the wake area. When the train runs at three speed levels of 400, 500 and 600 km·h^{-1}, respectively, the radiated energy of quadrupole source is 62.4%, 63.3% and 71.7%, respectively, which exceeds that of dipole sources.

Originality/value – This study can help understand the aerodynamic noise characteristics generated by the high-speed maglev train and provide a reference for the optimization design of its aerodynamic shape.

Keywords High-speed maglev train, Aerodynamic noise, Penetrable integral surface, Large eddy simulation, Speed level

Paper type Research paper

1. Introduction

With the rapid development of the transport system, people's requirements for travel speed are getting higher. When the speed is increased to above 400 km·h^{-1}, high-speed trains are

The research was supported by the National Key Research and Development Program (Grant No. 2020YFA0710903), the Financial Funding Project for Central Colleges and Universities (Grant No. 202045014) and the Science and Technology Research and Development Program of China State Railway Group Co., Ltd. (Grant No. P2019J008).

Railway Sciences
Vol. 2 No. 3, 2023
pp. 310-326
Emerald Publishing Limited
e-ISSN: 2755-0915
p-ISSN: 2755-0907
DOI 10.1108/RS-04-2023-0019

limited by the wheel-rail system and current collection conditions of pantograph catenary during operation. As a new means of transport, the maglev train is suspended on the track during operation and can reach higher operating speed compared with high-speed trains so that it has become a hot topic (Ding, Ge, Guo, Zhao, & Fu, 2020; Liang, Liu, Dong, Yang, & Tan, 2020). At present, the prototype of high-speed maglev train independently developed by China has been launched, with a design speed of 600 $km \cdot h^{-1}$, which can effectively fill the blank speed zone between high-speed railway and civil aviation transport, has a broad development prospect, and is of great significance for improving the high-speed transport system (Meng, Zhou, & Meng, 2020).

When the maglev train runs at a high speed, the aerodynamic effect around the train has a great impact on the stability and comfort of the train (Tian, 2019). Therefore, scholars at home and abroad have carried out relevant research on the aerodynamic performance of maglev trains. Tyll, Liu, and Schetz (1996) comprehensively studied the aerodynamic performance of TR06 maglev train model (scale: 1:12 based on the real train) with three-car formation at a speed of about 241.4 $km \cdot h^{-1}$ by using a wind tunnel with moving ground, and obtained the aerodynamic data of the train, which provided a reference basis for future research. Yao, Chen, Ding, and Pang (2021) used the improved vehicle modeling function (VMF) parametric method and the curved surface discrete method to carry out the parametric design on the nose of high-speed maglev train, and the aerodynamic drag coefficient of the whole train decreased by 19.2% after the optimized shape was used. Through a simulation study on the flow field characteristics of a high-speed maglev train on an open track at a speed of 600 $km \cdot h^{-1}$, Zhou, Li, Zhao, and Zhang (2020) found that the thickness of the side boundary layer of the car body increased significantly due to the impact of surface vortex structure shedding, many vortex structures were generated at the train shoulder and in the curved surface change area, and a pair of longitudinal vortexes rotating in the opposite direction appeared in the wake area.

There are few numerical simulation studies on aerodynamic noise of maglev trains in existing documents, most of which are experimental studies on aerodynamic noise of maglev trains. For example, Germany measured the passing noise level of TR08 train in the test lines, and obtained the A-weighting sound pressure levels of standard measuring points at a speed range of 200–400 $km \cdot h^{-1}$ for different track types (Barsikow *et al.*, 2002). Duan, Zhang, Zhu, and Qin (2010) used a multi-channel noise analysis system to collect and analyze the signals generated during the operation of medium and low speed maglev trains. The results showed that at the same speed level, the radiated noise of medium and low speed maglev trains was lower and more environmentally friendly than that of wheel-rail trains. Zhao, Sheng, Liu, and Mo (2005) conducted a field test on the running noise of maglev trains at a speed of 430 $km \cdot h^{-1}$ on the Shanghai maglev rail transit operation line, and the results showed that the main noise source of maglev train was aerodynamic noise, which was impulsive and intermittent, so the noise pollution to the environment on both sides of the track cannot be ignored. This is consistent with the experimental study results obtained by Chen, Tang, Huang, and Wang (2007) on the impact of Shanghai maglev trains on surrounding residents.

Due to the limitation of line conditions, the aerodynamic noise test of high-speed maglev train with a speed of 600 $km \cdot h^{-1}$ is not available yet. In addition, when the operating speed of the train exceeds 0.3 Ma, the energy contribution of quadrupole sources cannot be overlooked (Tan, Wang, Qian, Qin, & Lu, 2019). However, the test method is not practical for the in-depth study on the characteristics of the quadrupole sources. Therefore, numerical simulation is the main method to study the aerodynamic noise of a high-speed maglev train with a speed of 600 km h^{-1}.

Based on the Kirchhoff–Ffowcs Williams and Hawkings (K-FWH) equation and the large eddy simulation (LES) method, the aerodynamic excitation characteristics of maglev trains at a speed of 600 $km \cdot h^{-1}$ are discussed. The dipole and quadrupole effects of aerodynamic sound of high-speed maglev trains are numerically simulated and studied through the

reasonable establishment of penetrable integral surface, and the variation rules of aerodynamic noise characteristics of a train at different speed levels are obtained.

2. Mathematical physical model

2.1 Large eddy simulation (LES)

LES has good ability to capture vortex structures and flow field pulsation and is suitable for refined flow field simulation. In this paper, this method is used for simulation calculation. In previous research, Mare and Jones (2003), Menter, Kuntz, and Langtry (2003),Smagorinsky (1963) and Vasilyev, Lund, and Moin (2001) have provided detailed discussion in their work.

2.2 Sound radiation method of penetrable integral surface

Francescantonio derived the K-FWH equation (Williams & Hawkings, 1969) with a wider range of application from the traditional FW-H (Francescantonio, 1997) equation by using the basic idea of the Kirchhoff (Khromov, 1963) method. The far-field solution of the K-FWH differential equation can be obtained by using the free-space Green's function and the generalized function theory (Farassat, 1981).

The penetrable integral surface is a control surface including the main hydrodynamic sound sources established in the calculation domain, which does not affect the airflow. When the sound source surface is a solid surface in the flow field, the radiated noise of monopole and dipole source on the solid surface is obtained by integrating it with the K-FWH equation. The contributions of monopole source, dipole sources and quadrupole sources in the space covered by the integral surface can be obtained by integrating the penetrable integral surface deviating from the solid surface (Ikeda, Enomoto, Yamamoto, & Amemiya, 2012).

3. Simulation model

In this paper, a simplified maglev train is adopted. The train height $H = 0.5$ m is adopted as the characteristic length, the train width is $0.9H$, and the train length is $32H$. In order to study the contribution rate of each part to aerodynamic noise, the train is divided into head car streamlined part, head car, middle car 1, middle car 2, middle car 3, tail car and streamlined tail car along the length of the car. A simplified model with a scale of 1:8 is established, as shown in Figure 1.

The maglev trains generally run on elevated lines. The train and magnetic rail are located in the center of the calculation domain, as shown in Figure 2. In the x direction, the distance from the front nose to the entrance of the calculation domain is $20H$, and that from the tail to the exit of the calculation domain is $69H$.

Both the entrance face *ABCD* and the exit face *KLMN* of the calculation domain are set as the pressure far-field boundary; the four sides are set as the symmetrical boundary, so that the normal velocity of the side is 0, which eliminates the influence of the wall on the flow field while ensuring the full development of the flow field; the train surface is set to the non-slip boundary condition; the track is set to the moving solid boundary condition with a velocity consistent with the inflow velocity.

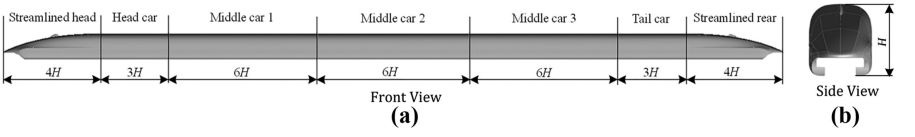

Figure 1.
High-speed maglev train model

Source(s): Authors own work

The pre-processing software integrated computer engineering and manufacturing code for computational fluid dynamics (ICEM CFD) is used to grid on and around the surface of the maglev train. The grid distribution is shown in Figure 3. The grid size of the streamlined nose is 3.75 mm, that of the head car and the tail car is 5 mm, and that of the middle car is 6.25 mm. In order to accurately describe the aerodynamic noise sources of surface dipoles, a boundary layer of tri-prism grids is added to the car body surface, and the thickness of the first layer of grids is 12.5 μm, with a growth rate of 1.2. Three densified areas of nested structure are set around the car body, with the maximum grid size of 15, 35 and 80 mm, respectively. The total number of grid cells is about 450 million. The average value of $Y+$ (non-dimensional distance from the center of mass of the first layer of grids to the wall) on the car body surface is less than 1, indicating that the grid size meets the basic requirements of numerical solution by LES.

For the simulation calculation, the train speed range is 400–600 km·h^{-1}, the Mach number is greater than 0.3, and the air compressibility effect is obvious. Therefore, the density-based implicit solution method is used to calculate the steady flow field, and the shear stress transfer (SST) $k-\omega$ turbulence model is used for numerical simulation. The convection term and dissipation term are both discretized by the second-order upwind scheme. Then, the Smagorinsky–Lilly-based LES model is used for LES transient calculation, and the Coupled

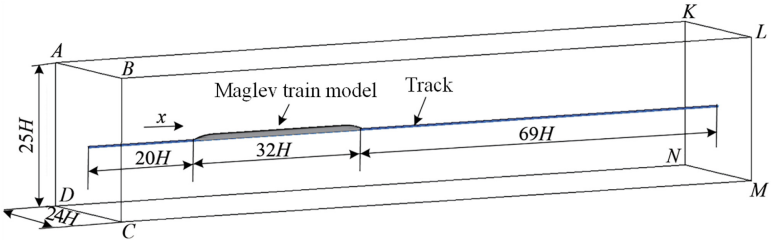

Source(s): Authors own work

Figure 2.
Simulation calculation domain

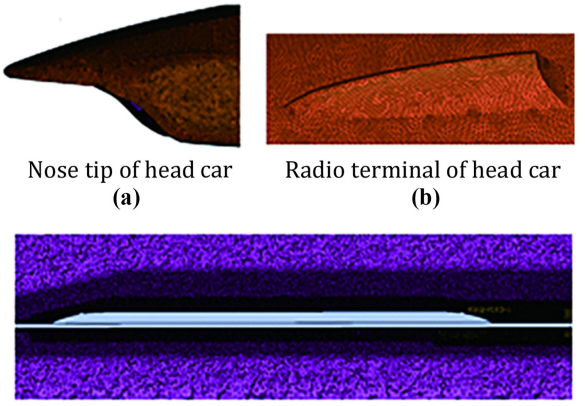

Source(s): Authors own work

Figure 3.
Schematic diagram of grids

algorithm is used to couple the pressure and velocity fields. The bounded second-order implicit scheme is used to discretize the time derivatives, and the bounded central difference is used to discretize the momentum equations. The unsteady calculation time step is taken as 5×10^{-5} s, with 30 iterations in each time step, and a total of 1×10^{4}-time steps are calculated. It can be judged whether the flow field is fully developed by monitoring the aerodynamic force of the train and the velocity change at 1 train length from the tail of the train.

4. Aerodynamic excitation characteristics

The pulsating pressure on the train surface is the key to the sound field calculation, so it is necessary to accurately simulate the pulsating flow field around the train (Tan, Yu, Tan, Yang, & Gao, 2021). The aerodynamic excitation characteristics of the maglev train are studied by analyzing the development of the boundary layer and the vortex structures around the train.

For analysis purposes, the flow field velocity V is dimensionless.

$$C_v = \frac{V}{V_{\text{in}}} \tag{1}$$

where C_v refers to the dimensionless velocity; V_{in} refers to the inflow velocity given by the entrance boundary.

Due to the viscosity of air, when the air flows over the surface of the car body, a boundary layer with a large velocity gradient is formed, and its thickness is defined as the vertical distance when the velocity in the normal direction of the wall is $0.99V_{\text{in}}$.

The nephogram of the boundary layer of the central symmetrical section of the train along the length of the train at a speed of 600 km h^{-1} is colored by C_v, as shown in Figure 4. It can be seen from Figure 4 that the airflow was blocked by the nose tip of the head car, so its velocity decreased rapidly, forming a stagnation area in this area. Then, the airflow moved backward along the car body. Due to the viscosity of air, a boundary layer with a large velocity gradient was formed on the surface of the car body, and it generated small disturbance when flowing through the radio terminal area of the head car. Subsequently, the boundary layer developed steadily along the car body, and its thickness increased continuously. Finally, after the airflow passed through the shoulder of the streamlined part of the tail car, the boundary layer was separated from the car body due to the variation of the curved surface. The radio terminal is located in the sensitive area of the separation, exacerbating the airflow disturbance in this area.

It can be seen that when the maglev train is running at a high speed, the spatial disturbance near the car body resulting from the separation of the boundary layer is mainly concentrated in the streamlined tail car and its wake area.

In order to show the characteristics of the transient flow field around the train, the second invariant of the velocity gradient tensor, namely Q criterion, is used to identify the vortex structures around the train. The expression of Q criterion is

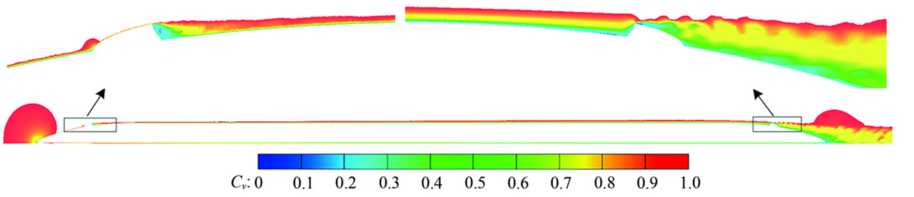

Figure 4.
Nephogram of boundary layer (at a speed of 600 km·h^{-1})

Source(s): Authors own work

$$Q = -\frac{1}{2}\left(\overline{S}_{ij}\overline{S}_{ij} - \overline{\Omega}_{ij}\overline{\Omega}_{ij}\right) \tag{2}$$

where $\overline{S}_{ij}$ and $\overline{\Omega}_{ij}$ refer to the symmetric and antisymmetric terms of the velocity gradient tensor, respectively.

The nephogram of three-dimensional vortex structures ($Q = 2 \times 10^5\ s^{-2}$) around the train at a speed of 600 $km \cdot h^{-1}$ is shown in Figure 5. It can be seen from Figure 5 that the vortex structures of the train are mainly distributed in the head car streamlined part, streamlined tail car and its wake area. Distributed in strips at the top of and on both sides of the head car streamlined part, the vortex structures develop backward along the car body and disappear at the shoulder position. In the arm area of the head car, after the airflow impacts the arms, part of the airflow flows to the narrow gap between the arms and the track, and part of the airflow develops backward along the side and bottom of the arms, forming a small-scale vortex structure shedding; the radio terminal of the head car is the only raised part in the streamlined part of the head car, and its structure features narrow upstream and wide downstream. The airflow impacts the tip of the radio terminal and moves backward along its surface, and then separates on its two sides to form two rows of vortex structures, which develop backward along the car body. On the surface of the streamlined tail car, the vortex structures are similar to those on the surface of the head car streamlined part, but the velocity amplitude is lower. The radio terminal of the tail car is symmetrical with the radio terminal of the head car. Downstream of the radio terminal of the tail car, the vortex structures shed from the tip of the radio terminal, forming C-shaped shedding vortexes with a downward opening. In the streamlined area of the tail car, due to the separation of the boundary layer from the car body, the airflow mixing effect is obvious, and vortex structures curling from the middle to the outside are formed in the wake area and develop downstream.

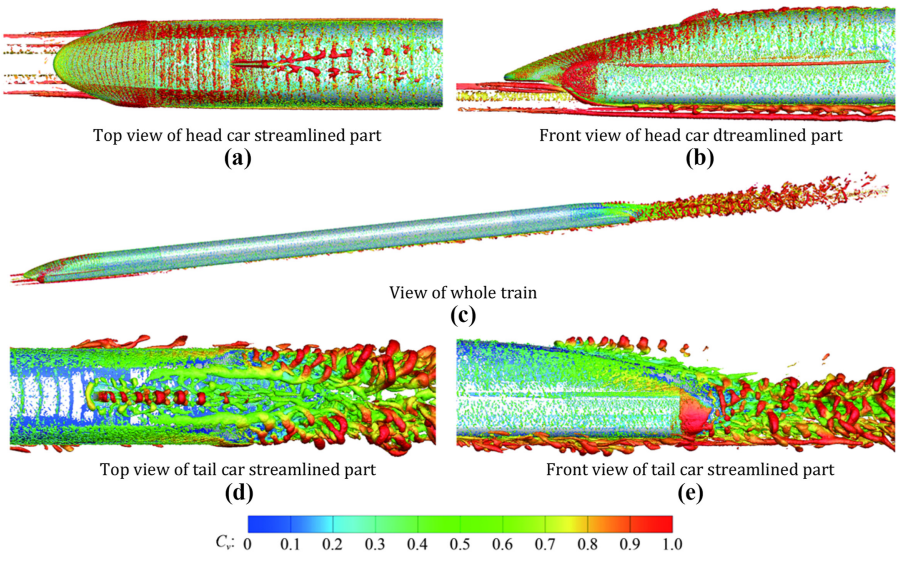

Source(s): Authors own work

Figure 5. Vortex structures around the train ($Q = 2 \times 10^5\ s^{-2}$)

5. Aerodynamic noise characteristics

5.1 Dipole source

The intensity of dipole sources on the train surface can be characterized by the root-mean-square p'_{rms} of the time gradient of the pulsating pressure on the train surface, and it is dimensionless to obtain its dimensionless value C_{rms}. The expressions are as follows:

$$p'_{rms} = \sqrt{\frac{1}{T}\int_0^T (p')^2 \mathrm{d}t} \tag{3}$$

$$C_{rms} = \frac{p'_{rms}}{p'_{rms-max}} \tag{4}$$

where T refers to the sampling time; p' refers to the pulsating pressure on the train surface; $p'_{rms-max}$ refers to the maximum root-mean-square of the time gradient of the pulsating pressure on the train surface.

The C_{rms} nephogram at a speed of 600 km·h^{-1} is shown in Figure 6. In the upper part of the car body, dipole sources are mainly distributed at the radio terminals of the head and tail cars and the nose tip of the streamlined tail car; at the bottom of the train, the intensity of dipole sources at the bottom of the arms of the head car streamlined part and the bottom of the nose tip of the streamlined tail car is relatively high, and the intensity of dipole sources at the bottom of the arms from the head car to the tail car increases backward along the car body.

To further determine the energy contribution of dipole source of each part of the train, the calculation formula for the power P_{source} of equivalent sound sources in each part is as follows

$$P_{source} \propto \overline{\left(\int_S \frac{\partial}{\partial t} p(\boldsymbol{y}) \mathrm{d}S(\boldsymbol{y})\right)^2} = \overline{\left(\frac{\partial}{\partial t}\int_S p(\boldsymbol{y}) \mathrm{d}S(\boldsymbol{y})\right)^2} \tag{5}$$

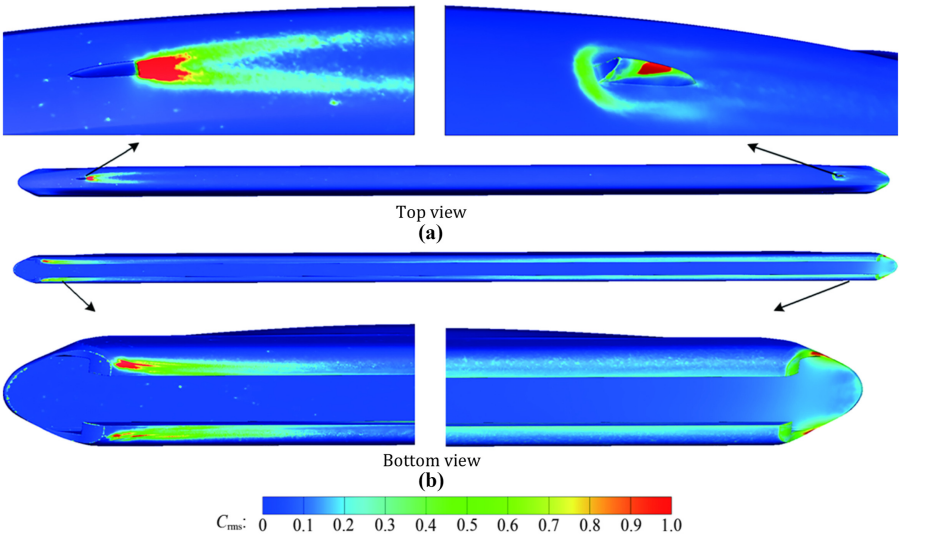

Figure 6.
C_{rms} nephogram (at a speed of 600 km·h^{-1})

Source(s): Authors own work

where $\boldsymbol{y}$ refers to the spatial coordinate vector of sound source; $\frac{\partial p(\boldsymbol{y})}{\partial t}$ refers to the time gradient of pulsating pressure on the train surface; t refers to time; S refers to the area of noise source.

The calculation result of the power of equivalent sound sources in each part is shown in Figure 7. It can be seen from Figure 7 that, as the speed increases, the energy of the dipole sources of the train also increases; at different speed levels, the energy of the dipole sources of the train shows a distribution characteristic of large at both ends and small in the middle; the energy of the dipole sources in the streamlined area of the tail car is the largest, followed by that in the streamlined area of the head car. From the head car to the middle car 3, the energy of the dipole sources shows an overall upward trend, indicating that the airflow disturbance in the boundary layer becomes stronger as the boundary layer develops downstream, which is consistent with the intensity distribution characteristics of the dipole sources of the train. Due to the small area of the car body, the source energy of the tail car is lower than that of the middle car 3.

To study the spectral characteristics of the dipole sources of the train, Fourier transform is used to convert the time domain data output by the sound field calculation into frequency domain data, and the pulsating pressure on the train surface–time gradient at different frequencies is obtained. Then, the power of equivalent sound sources of the train at different frequencies is obtained with formula (5). The power spectrum of equivalent sound sources with a large proportion of the energy of dipole sources in the head car streamlined part and the streamlined tail car is shown in Figure 8.

It can be seen from Figure 8 that the energy of the dipole sources in each part of the train shows a broadband characteristic, and the acoustic energy of each frequency band increases with the increase of speed, with the most obvious increase in the frequency band of 800–2,500 Hz. It can be seen from the spectrum curves of the head and the streamlined tail car that the peak characteristics at a speed range of 400–500 km h^{-1} are not obvious. However, when the speed is increased to 600 km h^{-1}, a single peak characteristic is obvious. The peak frequencies in the head and streamlined tail cars are 1,600 and 800 Hz, respectively.

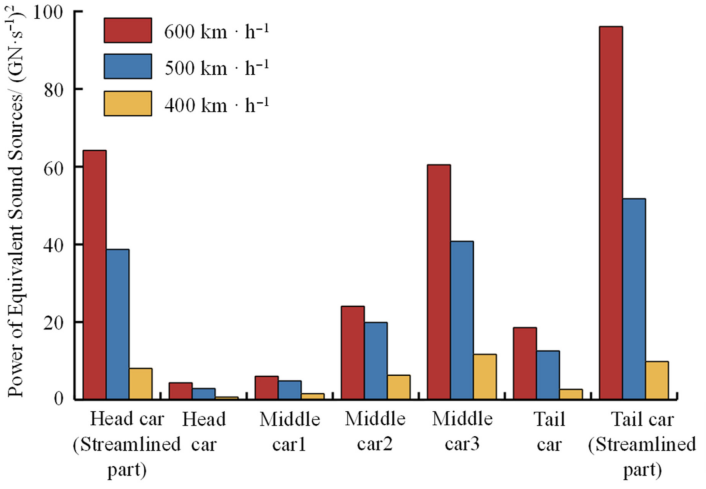

Source(s): Authors own work

Figure 7.
Power of equivalent sound sources in each part

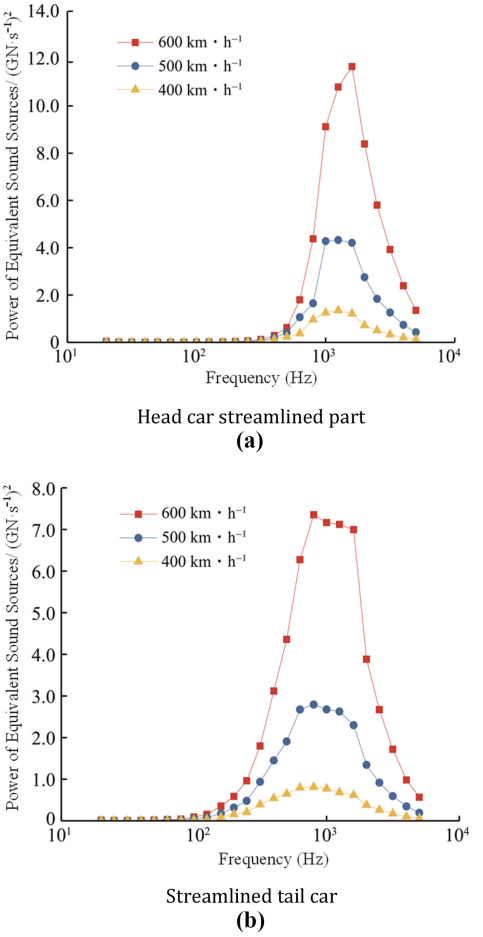

Figure 8.
Power spectrum of equivalent sound sources

Source(s): Authors own work

5.2 Far-field radiated noise

To study the radiated noise of the train, one measuring point is arranged every 5*H* at a distance of 6.25*H* and a height of 0.875*H* from the longitudinal symmetry plane of the train, and a total of 16 measuring points are arranged, as shown in Figure 9.

5.2.1 Establishment of penetration integral surface. Theoretically, as long as the integral surface is large enough to include all the disturbance sources, the loss of sound source energy can be avoided. However, this method will greatly increase the calculation amount and affect the calculation efficiency. Therefore, the integral surface is only established in the area where quadrupoles might be generated to ensure the calculation accuracy of the model. The generation of quadrupole sources is usually accompanied by strong vortex shedding (Li, Liang, Han, Quan, & Peng, 2020). According to the analysis of the aerodynamic excitation characteristics of the train, there is a strong spatial disturbance in the streamlined tail car and wake area with obvious vortex shedding. Therefore, a penetrable integral surface is established in the streamlined tail car and wake area.

The integral surface to be established should cover the main sound source area of the train as much as possible, while ensuring that the integral surface itself has no mass penetration (Tan *et al.*, 2019). As observed in Figure 4 that the boundary layer separation point is located behind the shoulder of the streamlined part, so the starting point of the integral surface is set at the shoulder of the streamlined part. The vorticity amplitude in the wake area of the train is extracted to reasonably determine the truncation position of the integral surface. The extraction position and the vorticity development curve obtained are shown in Figure 10. It can be seen from Figure 10 that the vorticity amplitude in the wake area fluctuates gently at the position $x = 50H$, and gradually tends to 0 afterwards.

As the end of the integral surface is located in the wake area of the train, the end of the integral surface is set at the position of $x = 62H$ to prevent mass penetration and pseudo sound at this position. According to the characteristic that the vortex structure in the streamlined area of the tail car diverges to two sides in the backward development process, the integral surface in this area adopts the form of narrow upstream and wide downstream. The specific dimension of the integral surface is shown in Figure 11.

Source(s): Authors own work

Figure 9.
Layout of far-field measuring points

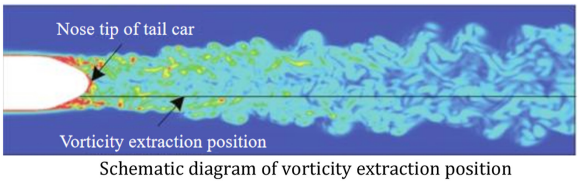

Schematic diagram of vorticity extraction position

(a)

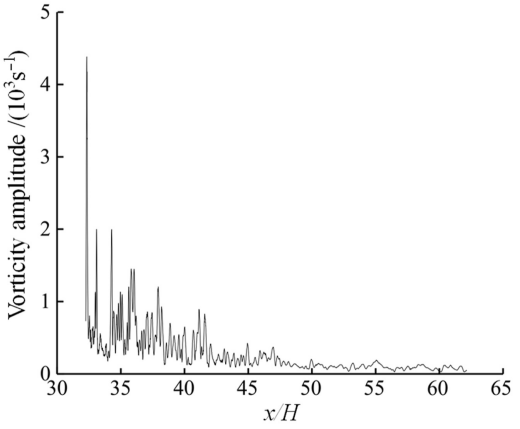

Vorticity development curve

(b)

Source(s): Authors own work

Figure 10.
Schematic diagram of vorticity development in wake area of the train

After the integral surface is established, in terms of the calculation of the radiated noise at the far-field measuring point, for the area covered by the integral surface, the integral surface is used as the sound source area for integral statistics; for the area not covered by the integral surface, the car body is used as the sound source area for integral statistics.

5.2.2 Verification of numerical simulation method. In order to verify the correctness of the above penetrable integral surface method, the aerodynamic noise test of maglev train was carried out in the acoustic wind tunnel of China Aerodynamics Research and Development Center, and the test results were compared with the simulation results.

The test model is a high-speed maglev train of three-car formation, with a scale of 1:8, a model height H_1 of 0.497 m, a width of $0.94H_1$ and a length of $19.7H_1$. The inflow velocity in the wind tunnel test is 300 km·h^{-1}. The wind tunnel test model established is shown in Figure 12.

Sixteen far-field microphones are arranged on the side of the model to measure the radiated noise of the test model. As shown in Figure 13, two rows are arranged vertically, the first row of microphones is $0.8H_1$ away from the floor, and the second row is $1.6H_1$ away from

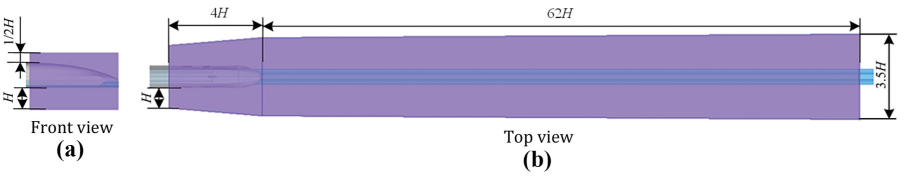

Figure 11.
Integral surface of streamlined tail car part

Source(s): Authors own work

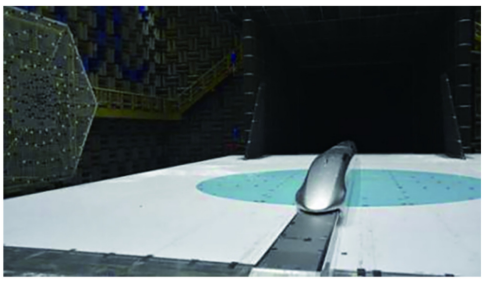

Figure 12.
Wind tunnel test model

Source(s): Authors own work

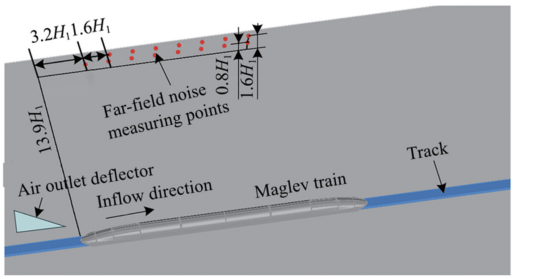

Figure 13.
Schematic diagram of microphone layout

Source(s): Authors own work

the floor; eight microphones are arranged in each row along the flow direction, with an axial spacing of $1.6H_1$, and the first microphone in the upstream is $3.2H_1$ away from the train nose; all microphone channels are collected synchronously, with a sampling frequency of 51.2 kHz and a sampling time of 90 s.

The corresponding numerical simulation model and calculation domain are established according to the wind tunnel test model and the scale of the wind tunnel. A penetrable integral surface is established in the streamlined area of the tail car by using the above integral surface establishment method, and the sound pressure level monitoring points are set at the corresponding positions. The sound pressure level of each measuring point is calculated with KFW-H equation.

At a train speed of 300 km·h^{-1}, the comparison results of radiated noise from wind tunnel test and numerical simulation are shown in Table 1. It can be seen from Table 1 that the maximum error of the first row of measuring points at a height of $0.8H_1$ from the floor is 1.7 dB; the error between the simulation value and the test value of the second row of measuring points at a height of $1.6H_1$ from the floor is within 0.9 dB; the difference between wind tunnel test data and simulation data is within 2 dB, indicating that the two results agree well.

It can be seen that the simulation method proposed above considering the noise radiation of quadrupole sources has good accuracy.

5.2.3 Radiated noise results. A-weighting is a commonly used frequency weighting method, which is closest to the subjective perception of noise by the human ear and is often used as an important indicator for noise evaluation. The A-weighting results are used for the radiated noise of the train to more visually represent the impact of the radiated noise of the maglev train on the environment. The radiated noise results of far-field measuring points under the two integration schemes are shown in Figure 14, in which for Scheme 1, the car body is taken as the sound source surface for integral calculation; for Scheme 2, the penetrable integral surface is taken as the sound source surface in the streamlined area of the tail car, while the car body is taken as the sound source surface in other parts. It can be seen from Figure 14 that the sound pressure level of each measuring point increases after the integral surface is established, indicating that the integral surface can effectively capture the quadrupole sources in the streamlined area of the tail car; the closer the measuring point is to the wake area, the more obvious the sound pressure level increases.

The spectrum curve of peak measuring point 10 is shown in Figure 15. It can be seen from Figure 15 that the sound pressure levels of far-field radiated noise measuring points in low frequency band are higher than those of the car body after the integral surface is established at the tail of the train, indicating that the radiated noise energy of quadrupole sources captured by the integral surface are mainly concentrated on the low frequency band; in the frequency band higher than 2,500 Hz, the sound pressure levels are lower than those of the car body, indicating that the energy of the dipole sources on the car body surface is lost in the

Channel no.	First row ($0.8H_1$ from the floor) Test value	First row ($0.8H_1$ from the floor) Simulation calculation value	Second row ($1.6H_1$ from the floor) Test value	Second row ($1.6H_1$ from the floor) Simulation calculation value
1	88.6	88.3	88.8	88.1
2	88.6	89.1	88.9	88.9
2	88.8	89.8	89.4	89.6
4	89.8	90.5	90.3	90.3
5	89.9	91.2	90.3	91.0
6	89.6	91.3	90.2	91.1
7	89.9	91.2	90.1	91.0
8	89.9	91.2	90.3	91.0

Source(s): Author's own work

Table 1. Comparison results of radiated noise between numerical simulation and wind tunnel test at a train speed of 300 km·h^{-1} (unit: dB)

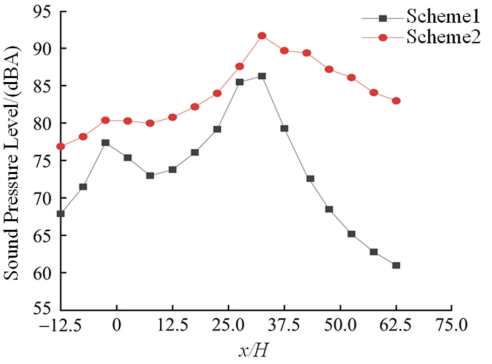

Source(s): Authors own work

Figure 14.
Sound pressure level of far-field radiated noise

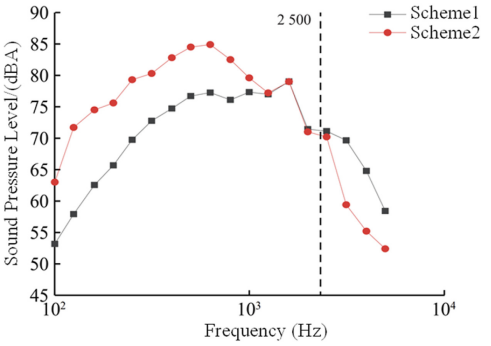

Source(s): Authors own work

Figure 15.
Radiated noise spectrum curve (measuring point 10)

process of transmitting to the integral surface, which may be caused by the filtering effect of the grid. However, the proportion of sound energy in the frequency band above 2,500 Hz is relatively small, so the loss of some sound energy in this frequency band has little influence on the statistics of the contribution of dipole sources of the car body. Hence, the integral surface can well capture the quadrupole sources in streamlined tail car and its wake area.

The radiated noise of the train at different speed levels is further studied by using the above integral surface schemes. The results of far-field radiated noise levels of dipole sources of the car body at a speed range of 400–600 km·h^{-1} are shown in Figure 16 (a). The variation rules of sound pressure levels at the far-field measuring points at a speed range of 400–600 km·h^{-1} are basically consistent, and there is a small bulge at the upstream measuring point 3; the maximum sound pressure level is obtained at the measuring point 10, which is 73.5 dB (A), 80.1 dB (A) and 86.3 dB (A), respectively. After the integral surface is established in the streamlined area of the tail car, the sound pressure level results of the far-field measuring points are shown in Figure 16 (b). The variation rule of far-field radiated noise is similar to that of the radiated noise of the car body, showing double peak characteristics, but the decline trend of sound pressure levels at the measuring points behind the nose tip of the tail car is obviously slower; the maximum sound pressure level of radiated noise is still at the measuring point 10, which is 78.3 dB (A), 84.9 dB (A) and 91.7 dB (A), respectively.

The average value of far-field radiated noise of the train is calculated as follows:

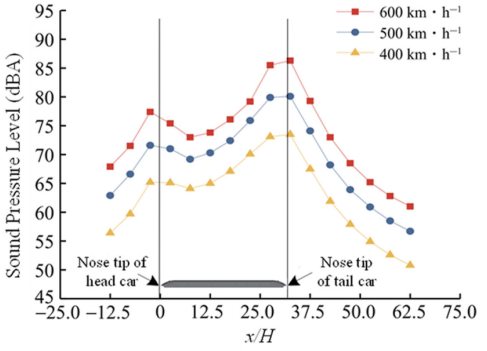

Car body (A-weighting)

(a)

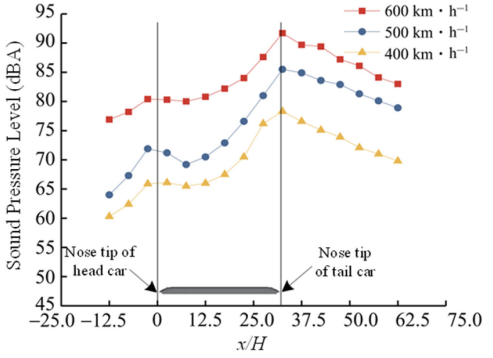

Integral surface (A-weighting)

(b)

Source(s): Authors own work

Figure 16.
Far-field radiated noise level

$$I = 10^{\frac{S_{PL}}{10}} \tag{6}$$

where I refers to the radiated noise energy; S_{PL} refers to the sound pressure level of the measuring point.

Formula (6) is used to calculate the average value of far-field radiated noise of the train, and the results are shown in Table 2. At three speed levels of 400, 500 and 600 km·h^{-1}, the average values of radiated noise of the car body are 78.7 dB (A), 85.1 dB (A) and 90.4 dB (A), respectively. After the integral surface is established, the average values of far-field radiated noise are 82.9 dB (A), 89.5 dB (A) and 95.9 dB (A), respectively.

The proportion of radiated noise energy of quadrupole sources at different speed levels is counted as follows:

$$W_{\text{quadrupole}} = \frac{(I_{\text{integral surface}} - I_{\text{car body}})}{I_{\text{integral surface}}} \times 100\% \tag{7}$$

where $W_{quadrupole}$ refers to the proportion of the radiated noise energy of quadrupole sources in the far-field radiated noise energy; $I_{car\ body}$ refers to the far-field radiated noise energy without integral surface; $I_{integral\ surface}$ refers to the far-field radiated noise energy with integral surface.

The statistics of the proportion of radiated noise energy of quadrupole sources at different speed levels according to formula (7) show that the proportion of radiated noise energy of quadrupole sources at three speed levels of 400, 500 and 600 is 61.7%, 63.3% and 71.1%, respectively.

It can be seen that when the train speed exceeds 400 km·h^{-1}, the radiated noise energy of quadrupole sources will exceed that of dipole sources, and the contribution of quadrupole sources will increase with the increase of train speed.

6. Conclusions

(1) The spatial disturbance around the maglev train results from the separation of the boundary layer in the streamlined area of the tail car and is mainly concentrated on the streamlined tail car and its wake area.

(2) In the speed range of 400–600 km h^{-1}, the energy of dipole sources on the train surface shows broadband characteristics, mainly distributed in the streamlined area of the tail car, followed by the streamlined area of the head car; the energy of quadrupole sources are mainly concentrated on the low frequency band, that is, in the streamlined tail car and its wake area.

(3) At different speeds, the distribution rules of radiated noise levels of dipole sources are similar, and small fluctuations occur near the corresponding measuring points of the nose tips of both the head car and the tail car; the maximum sound pressure level occurs at measuring point 10, 32.5H away from the nose tip of the head car. The variation rule of radiated noise is basically unchanged with the quadrupole sources considered, but the sound pressure level of each measuring point increases. At three speed levels of 400, 500 and 600 km·h^{-1}, the average sound pressure levels of far-field measuring points increase by 4.2 dB(A), 4.4 dB (A) and 5.5 dB (A), respectively.

(4) When the operating speed of maglev train exceeds 400 km·h^{-1}, the radiated noise energy of quadrupole sources will exceed that of dipole sources. With the increase of speed, the average energy of measuring points increases, and the proportion of energy of quadrupole sources at measuring points in the wake area also increases. At three speed levels of 400, 500 and 600 km·h^{-1}, the proportion of the radiated noise energy of quadrupole sources is 62.4%, 63.3% and 71.7%, respectively.

(5) The established numerical simulation model of aerodynamic noise can better capture the quadrupole sources near the car body, which is of great significance for further understanding the aerodynamic noise characteristics of high-speed maglev trains and can provide reference for the aerodynamic shape optimization of maglev trains.

Table 2. Average value of radiated noise at measuring points

Integral scheme	Average value of radiated noise at different speed levels/dB (A)		
	400 km·h^{-1}	500 km·h^{-1}	600 km·h^{-1}
Car body	78.7	85.1	90.4
Integral surface	82.9	89.5	95.9

Source(s): Author's own work

References

Barsikow, B., Disk, D. R., Hanson, C. E., Hellmig, M., Joshi, A., Mauri, R., and ... Valihura, P. (2002). *Noise characteristics of the transrapid TR08 maglev system* (pp. 32–69). Washington D.C: Federal Railroad Administration.

Chen, X., Tang, F., Huang, Z., & Wang, G. (2007). High speed maglev noise impacts on residents: A case study in Shanghai. *Transportation Research Part D: Transport and Environment*, *12*(6), 437–448.

Ding, S., Ge, J., Guo, J., Zhao, Y., & Fu, S. (2020). Noise emission assessment and countermeasures of high speed maglev system. *Electric Drive for Locomotives*, 6, 6–9.

Duan, C., Zhang, H., Zhu, Y., & Qin, Q. (2010). Noises of middle-low-speed maglev vehicles. *Applied Acoustics*, *29*(3), 184–188.

Farassat, F. (1981). Linear acoustic formulas for calculation of rotating blade noise. *AIAA*, *19*(9), 1122–1130.

Francescantonio, P. (1997). A new boundary integral formulation for the prediction of sound radiation. *Journal of Sound and Vibration*, *202*(4), 491–509.

Ikeda, T., Enomoto, S., Yamamoto, K., & Amemiya, K. (2012). *Quadrupole effects in the ffowcs williams-hawkings equation using permeable control surface*. In: *18th AIAA/CEAS aeroacoustics conference (33rd AIAA Aeroacoustics Conference)*. Colorado Springs, CO. Reston, Virigina: AIAA.

Khromov, V. A. (1963). Generalization of Kirchhoff's theorem for the case of a surface moving in an arbitrary way. *Soviet Physics Acoustics*, *9*, 68–71.

Li, R., Liang, W., Han, W., Quan, H., & Peng, G. (2020). Investigation of turbulence-induced quadrupole source acoustic characteristics of a three-dimensional hydrofoil. *Modern Physics Letters B*, *34*(23), 2050145.

Liang, X., Liu, H., Dong, T., Yang, Z., & Tan, X. (2020). Aerodynamic noise characteristics of high-speed train foremost bogie section. *Journal of Central South University*, *27*(6), 1802–1813.

Mare, L. D., & Jones, W. P. (2003). LES of turbulent flow past a swept fence. *International Journal of Heat and Fluid Flow*, *24*(4), 606–615.

Meng, S., Zhou, D., & Meng, S. (2020). Effect of rail gap on aerodynamic performance of maglev train. *Journal of Central South University: Science and Technology*, *51*(12), 3537–3545.

Menter, F. R., Kuntz, M., & Langtry, R. (2003). Ten years of industrial experience with the SST turbulence model. *Heat and Mass Transfer*, *4*(1), 625–632.

Smagorinsky, J. (1963). General circulation experiments with the primitive equations. *Monthly Weather Review*, *91*(3), 99–164.

Tan, X., Wang, T., Qian, B., Qin, B., & Lu, Y. (2019). Aerodynamic noise simulation and quadrupole noise problem of 600 km/h high speed train. *IEEE Access*, *7*, 66–75.

Tan, X., Yu, Z., Tan, X., Yang, Z., & Gao, Z. (2021). Flow field structure and aerodynamic noise source of high speed train on open track and in tunnel. *China Railway Science*, *42*(1), 95–104.

Tian, H. (2019). Review of research on high speed railway aerodynamics in China. *Transportation Safety and Environment*, *1*(1), 1–21.

Tyll, J. S., Liu, D., & Schetz, J. A. (1996). Experimental studies of magnetic levitation train aerodynamics. *AIAA Journal*, *34*(12), 2465–2470.

Vasilyev, O. V., Lund, T. S., & Moin, P. (2001). A general class of commutative filters for LES in complex geometries. *Journal of Computational Physics*, *146*(1), 82–104.

Williams, J. E. F., & Hawkings, D. L. (1969). Sound generation by turbulence and surfaces in arbitrary motion. *Philosophical Transactions of the Royal Society of London, Series A Mathematical and Physical Sciences*, *264*(1151), 321–342.

Yao, S., Chen, D., Ding, S., & Pang, S. (2021). Multi-objective aerodynamic optimization design of high speed maglev train nose. *China Railway Science*, *42*(2), 98–106.

Zhao, Y., Sheng, S., Liu, H., & Mo, F. (2005). Measurement and analysis of noise from running maglev systems. *Journal of Tongji University: Natural Science*, *33*(6), 768–771.

Zhou, P., Li, T., Zhao, C., & Zhang, J. (2020). Numerical study on the flow field characteristics of the new high speed maglev train in open air. *Journal of Zhejiang University: Science A*, *21*(5), 366–381.

Corresponding author
Guangjun Gao can be contacted at: gjgao@csu.edu.cn